

# Communication-Less Reactance Compensation Using PWM-Controlled Switched Capacitors for Wireless Power Transfer

Ryo Matsumoto, *Student Member, IEEE*, Toshiyuki Fujita, *Member, IEEE*,  
and Hiroshi Fujimoto, *Senior Member, IEEE*

**Abstract**—Self-inductance variations caused by component tolerance and aging decrease the efficiency of wireless power transfer (WPT) systems. This paper deals with this issue by compensating for the self-inductance variations using pulsewidth modulation controlled switched capacitors. Previous methods relied on wireless communication between the transmitter (Tx) and receiver (Rx) to control the variable capacitors, which is not a feasible approach when considering practical constraints. This paper proposes a control scheme in which the switched capacitors are controlled simultaneously by separate closed-loops on the Tx and Rx sides, thus eliminating wireless communication. The control scheme is based on a unique condition for perfect resonance derived by focusing on the output power of the WPT circuit. This paper also points out the necessity to compensate for the self-inductance variations of both the Tx and Rx coils to achieve maximum AC/AC efficiency in battery charging applications. Furthermore, the proposed control scheme incorporates the soft switching condition of the inverter to improve the DC/DC efficiency. Experimental results of a 1-kW prototype show that the switched capacitors can flexibly adapt to the self-inductance variations and improve the AC/AC efficiency and DC/DC efficiency by up to 3.04% and 8.63%, respectively.

**Index Terms**—Switched capacitor, self-tuning, resonant frequency, component tolerance, wireless power transfer (WPT).

## I. INTRODUCTION

WIRELESS power transfer (WPT) is considered as a safe and convenient way to provide power to a wide range of applications, such as consumer electronics [1] and electric vehicles [2]. Among several types of WPT technologies, the magnetic resonance coupling can achieve high efficiency and high power over large air gaps, thus maximizing the benefits of WPT [3]. These attractive features are typically achieved by canceling the reactance of the transmitter (Tx) and receiver (Rx) coils with compensation capacitors [4], [5].

However, in practical WPT applications, the following factors cause the parameters of the coils and capacitors to

vary from their designed values, thus preventing the reactance from being completely compensated. The first factor is the manufacturing tolerance and aging of the coils and capacitors. The manufacturing errors of mass-produced electronic components are inevitable. The second factor is the variation in the relative position of the Tx and Rx coils. The ferrite block and aluminum shield equipping the Tx coil affect the self-inductance of the Rx coil, and vice versa. This causes the self-inductance of the Tx and Rx coils to vary depending on their relative position [6], [7]. The third factor is the existence of other magnetic and conductive materials in the surrounding environment [8], [9]. For instance, if the Tx and Rx pads are installed near structures containing ferrous materials, the self-inductance of the coils will be affected.

By actively compensating the unnecessary reactance, the system can maintain the ideal performance even when the parameters of circuit components vary from their designed values. In the literature, several methods have been proposed to accomplish this goal using variable capacitors [10]–[18] and active rectifiers [19]–[22].

In [10]–[12], the resonance condition is maintained by switching the series and parallel connection of multiple capacitors. However, this method requires numerous switches and capacitors which increase the volume and cost of the system.

Several subsequent studies [13]–[18] have adopted variable capacitor circuits in which the equivalent capacitance is controlled by the gate signals of the MOSFETs. In [14], a pulsewidth modulation (PWM) controlled switched capacitor is adopted on the Tx side to compensate for the self-inductance variation of the Tx coil. In [15], the self-inductance variation of the Rx coil is compensated by a PWM-controlled switched capacitor on the Rx side. However, the studies in [14], [15] do not consider the scenario where the self-inductance of the Tx and Rx coils vary simultaneously. The studies in [16]–[18] adopt switch-controlled capacitors (SCCs) to compensate for the self-inductance variations of both the Tx and Rx coils. However, in [16], the control scheme for the Rx side SCC has not been investigated. In [17], the SCCs are controlled based on parameter recognition which is a complicated procedure and requires several circuit parameters to be pre-measured. The control scheme in [18] requires wireless communication to obtain the amplitude of the Tx current on the Rx side. However, wireless communication increases the complexity of the system and entails the risk of communication failures, packet losses, and delays.

Manuscript received November 17, 2022; revised February 6, 2023; April 1, 2023; and XXXXXXXXXXXX; accepted XXXXXXXXXXXX. Date of publication XXXXXXXXXXXX; date of current version XXXXXXXXXXXX. This work was supported in part by JST MIRAI (JPMJMI21E2), JSPS KAKENHI (JP18H03768), JST CREST (JPMJCR15K3), and CMK CORPORATION. This paper was presented in part at the Wireless Power Week (WPW), Bordeaux, France, July 5-8, 2022. Recommended for publication by Associate Editor XXXXXXXXXXXX. (*Corresponding author: Ryo Matsumoto.*)

The authors are with the Department of Advanced Energy, Graduate School of Frontier Sciences, The University of Tokyo, Chiba 277-8561, Japan (e-mail: matsumoto.ryo19@ae.k.u-tokyo.ac.jp; t-fujita@edu.k.u-tokyo.ac.jp; fujimoto@k.u-tokyo.ac.jp).

Other studies have adopted methods to control the phase shift angle of the active rectifier [19]–[21]. However, these methods can only compensate for the unnecessary reactance in the Rx circuit. In order to compensate for the unnecessary reactance in both the Tx and Rx circuits, an additional degree of freedom is required.

In [22], the frequency of the inverter and the phase shift angle of the semi-bridgeless active rectifier are controlled to compensate for the self-inductance variations of the Tx and Rx coils. In [23], [24], variable capacitors are adopted to maintain the resonance condition in multi-receiver WPT systems. The phase difference between the Tx and Rx currents plays an important role in the control schemes in [22]–[24]. Wireless communication is required to compare the instantaneous phase of the Tx and Rx currents. However, this is not a practical solution when considering the latency of wireless communication, as discussed in Section II-A.

In practical WPT applications, the coils and capacitors of both the Tx and Rx sides are subject to parameter variations. However, none of the previous studies have proposed methods to simultaneously compensate for the unnecessary reactance in the Tx and Rx circuits without wireless communication.

This paper proposes a control scheme for PWM-controlled switched capacitors to compensate for the self-inductance variations of the Tx and Rx coils without wireless communication. The control scheme is based on a unique condition for perfect resonance derived through the steady-state analysis of the WPT circuit. The information of the voltage and current phase of the Tx circuit is used to control the Tx side switched capacitor. On the other hand, the information of the output power is used to control the Rx side switched capacitor. The control scheme has the following advantages.

- 1) The self-inductance variations of the Tx and Rx coils can be simultaneously compensated.
- 2) Wireless communication is not required, since the switched capacitors are controlled by separate closed-loops on the Tx and Rx sides.

The basic idea of the control scheme was presented in our recent conference paper [25]. However, the control scheme was derived under several specific assumptions in order to simplify the analysis. Therefore, the generality of the proposed control scheme is clarified in this paper through a comprehensive analysis of the WPT circuit. Moreover, in [25], the optimal condition in terms of the end-to-end system efficiency was not investigated. This paper proposes an updated version of the control scheme in which the inverter efficiency is improved without sacrificing the AC/AC efficiency. This paper also includes experimental results obtained under diverse patterns of self-inductance variations in order to demonstrate the versatility of the control scheme.

The rest of this paper is structured as follows: Section II discusses the conditions for perfect resonance and derives a unique condition which is the underlying principle of the proposed control scheme. Section III describes the proposed control scheme in detail and explains how it can be further modified to improve the end-to-end system efficiency. Section IV presents the experimental results of a 1-kW prototype. Finally, Section V draws the conclusion.

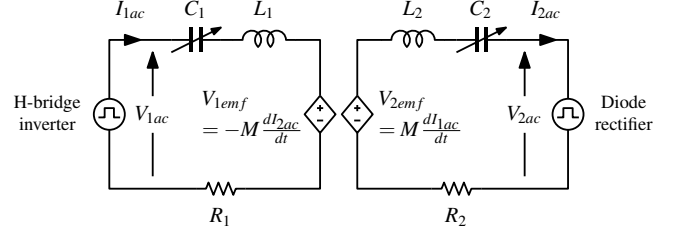


Fig. 1. Simplified model of a S-S compensated WPT circuit adopting variable capacitors.

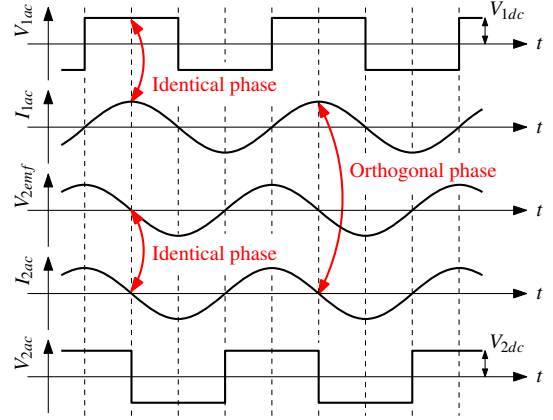


Fig. 2. Waveforms of  $V_{1ac}$ ,  $I_{1ac}$ ,  $V_{2emf}$ ,  $I_{2ac}$ , and  $V_{2ac}$  under the perfect resonance condition.

## II. CONDITIONS FOR PERFECT RESONANCE

This section focuses on the problem of how to determine whether or not the self-inductance variations are perfectly compensated by the variable capacitors. This problem is referred to as the condition for perfect resonance and formulates the underlying principle of the proposed control scheme. In Section II-A, conventional conditions for perfect resonance and their major drawbacks are described. In Section II-B, a unique condition for perfect resonance is derived to overcome the drawbacks of the conventional methods.

### A. Conventional Conditions for Perfect Resonance

Fig. 1 shows a simplified model of a S-S compensated WPT circuit. Variable capacitors are adopted instead of passive capacitors to compensate for the self-inductance variations of the Tx and Rx coils.  $L$ ,  $C$ , and  $R$  with subscripts 1 and 2 represent the coil's self-inductance, the variable capacitance, and the equivalent series resistance (ESR) of the Tx and Rx sides.  $M$  represents the mutual inductance between the Tx and Rx coils.  $V_{1ac}$  and  $V_{2ac}$  represent the terminal voltage of the inverter and rectifier.  $I_{1ac}$  and  $I_{2ac}$  represent the Tx and Rx currents.  $V_{1emf}$  and  $V_{2emf}$  represent the electromotive force induced in the Tx and Rx coils.

It is well known that high efficiency and high power are achieved under the perfect resonance condition:

$$\omega = \frac{1}{\sqrt{L_1 C_1}} = \frac{1}{\sqrt{L_2 C_2}} \quad (1)$$

where  $\omega$  is the operating angular frequency of the inverter [4]. When  $L_1$  and  $L_2$  vary from their designed values, the

optimal condition can be maintained by controlling  $C_1$  and  $C_2$  to satisfy (1). However, this requires the values of  $L_1$  and  $L_2$  to be measured beforehand using external equipments. Since this is not a practical solution, an alternative information to evaluate the resonance condition is necessary.

The most basic approach is to use the information of the voltage phase and the current phase. Fig. 2 shows the waveforms of  $V_{1ac}$ ,  $I_{1ac}$ ,  $V_{2emf}$ ,  $I_{2ac}$ , and  $V_{2ac}$  under the perfect resonance condition in (1). It is well known that under the optimal condition, the phase of  $V_{1ac}$  and  $I_{1ac}$  become identical, and the phase of  $V_{2emf}$  and  $I_{2ac}$  become identical as well [21]. Therefore, the condition for perfect resonance can be redescribed as:

$$\angle \dot{V}_{1ac} = \angle \dot{I}_{1ac} \wedge \angle \dot{V}_{2emf} = \angle \dot{I}_{2ac}. \quad (2)$$

In other words, the perfect resonance condition can be achieved by controlling  $C_1$  and  $C_2$  to satisfy (2). However, this is not a practical solution either since  $V_{2emf}$  cannot be measured directly.

It is also well known that when the circuit is in perfect resonance, the phase of  $V_{1ac}$  and  $I_{1ac}$  become identical, and the phase of  $I_{2ac}$  leads  $I_{1ac}$  by  $90^\circ$  [22]–[24]. Therefore, the condition for perfect resonance can be redescribed as:

$$\angle \dot{V}_{1ac} = \angle \dot{I}_{1ac} \wedge \angle \dot{I}_{2ac} = \angle \dot{I}_{1ac} + \frac{\pi}{2}. \quad (3)$$

$V_{1ac}$ ,  $I_{1ac}$ , and  $I_{2ac}$  are measurable. However, wireless communication between the Tx and Rx sides is required to obtain the phase difference between  $I_{1ac}$  and  $I_{2ac}$ . Wireless communication increases the complexity of the system and entails the risk of communication failures. Moreover, it is impractical to compare the instantaneous phase of  $I_{1ac}$  and  $I_{2ac}$  when considering the latency of wireless communication. For instance, the typical operating frequency for wireless EV charging is 85 kHz. On the other hand, the latency of wireless communication is in the order of milliseconds [26], which is several orders of magnitude longer than the period of an 85 kHz sine wave. In order to control the variable capacitors, a condition for perfect resonance which can be evaluated without wireless communication is necessary.

### B. Proposed Condition for Perfect Resonance

Another unique condition for perfect resonance can be derived by focusing on the output power of the WPT circuit. The condition for perfect resonance can be redescribed as:

$$\angle \dot{V}_{1ac} = \angle \dot{I}_{1ac} \wedge P_2 = \min \left\{ P_2 \mid \angle \dot{V}_{1ac} = \angle \dot{I}_{1ac} \right\}. \quad (4)$$

where  $P_2$  represents the output power of the WPT circuit. In fact, the perfect resonance condition is achieved when the output power is minimized under  $\angle \dot{V}_{1ac} = \angle \dot{I}_{1ac}$ . This condition is equivalent to the conditions in (1)–(3). The derivation of (4) is explained in the remainder of this section.

Under the fundamental harmonic approximation, the input power and the output power are given by:

$$P_1 = R_1 |\dot{I}_{1ac}|^2 + R_2 |\dot{I}_{2ac}|^2 + |\dot{V}_{2ac}| |\dot{I}_{2ac}|, \quad (5)$$

$$P_2 = |\dot{V}_{2ac}| |\dot{I}_{2ac}|. \quad (6)$$

The reactance of the Tx circuit and the reactance of the Rx circuit are defined as:

$$X_1 := \omega L_1 - \frac{1}{\omega C_1}, \quad X_2 := \omega L_2 - \frac{1}{\omega C_2}. \quad (7)$$

$X_1$  and  $X_2$  are equal to zero under the perfect resonance condition. Based on this definition,  $p_1$  and  $p_2$  are defined as per-unit expressions of  $P_1$  and  $P_2$  as:

$$p_1 := \frac{P_1(X_1, X_2)}{P_1(X_1=0, X_2=0)}, \quad p_2 := \frac{P_2(X_1, X_2)}{P_2(X_1=0, X_2=0)}. \quad (8)$$

$p_1$  and  $p_2$  quantify how much the input power and the output power fluctuate from their optimal values according to  $X_1$  and  $X_2$ . In addition,  $q_1$ ,  $q_2$ ,  $x_1$ , and  $x_2$  are defined as non-dimensional expressions of  $R_1$ ,  $R_2$ ,  $X_1$ , and  $X_2$  as:

$$q_1 := \frac{\omega \sqrt{L_1 L_2}}{R_1}, \quad q_2 := \frac{\omega \sqrt{L_1 L_2}}{R_2}, \quad (9)$$

$$x_1 := \frac{X_1}{\omega \sqrt{L_1 L_2}}, \quad x_2 := \frac{X_2}{\omega \sqrt{L_1 L_2}}. \quad (10)$$

$q_1$  and  $q_2$  represent the quality factor of the Tx and Rx coils.  $x_1$  and  $x_2$  represent the percentage of self-inductance variations.  $R_1$ ,  $R_2$ ,  $X_1$ , and  $X_2$  are normalized by  $\omega \sqrt{L_1 L_2}$  to express  $p_1$  and  $p_2$  in terms of completely non-dimensional parameters. In this way,  $p_1$  and  $p_2$  can be calculated without specifying the values of  $L_1$ ,  $L_2$ ,  $R_1$ ,  $R_2$ , and so on, thus performing the analysis in a generalized manner.

The coupling coefficient between the Tx and Rx coils is defined as  $k := \frac{M}{\sqrt{L_1 L_2}}$ .

From Fig. 2, the root mean square values of  $V_{1ac}$  and  $V_{2ac}$  can be expressed in terms of  $V_{1dc}$  and  $V_{2dc}$  as:

$$|\dot{V}_{1ac}| = \frac{2\sqrt{2}}{\pi} V_{1dc}, \quad |\dot{V}_{2ac}| = \frac{2\sqrt{2}}{\pi} V_{2dc}. \quad (11)$$

In practical WPT applications, the inverter and rectifier are usually interfaced to constant voltage DC buses. In wireless EV charging, the rectifier is directly connected to the battery, or a DC/DC converter is connected between the rectifier and the battery [27]. Assuming that the output voltage of the battery is constant,  $V_{1dc}$  and  $V_{2dc}$  can be treated as constants when analyzing the circuit characteristics [28], [29]. Therefore,  $\lambda$  is defined as the ratio of  $V_{1dc}$  and  $V_{2dc}$  as:

$$\lambda := \frac{V_{1dc}}{V_{2dc}}. \quad (12)$$

By solving Kirchhoff's voltage law (KVL) equations derived from Fig. 1 with respect to (5)–(12),  $p_1$  and  $p_2$  can be expressed in terms of non-dimensional parameters as:

$$p_1 = \frac{\left( \frac{1}{q_1 q_2} + k^2 \right) \left[ \frac{x_2^2}{q_1} + \left( \frac{1}{q_2} + \zeta \right) \left( \frac{\zeta}{q_1} + \frac{1}{q_1 q_2} + k^2 \right) \right]}{\zeta^2 k^2 \left( \lambda k + \frac{\lambda^2}{q_2} \right)}, \quad (13)$$

$$p_2 = \frac{\frac{1}{q_1 q_2} + k^2}{\zeta \left( \lambda k - \frac{1}{q_1} \right)} \quad (14)$$

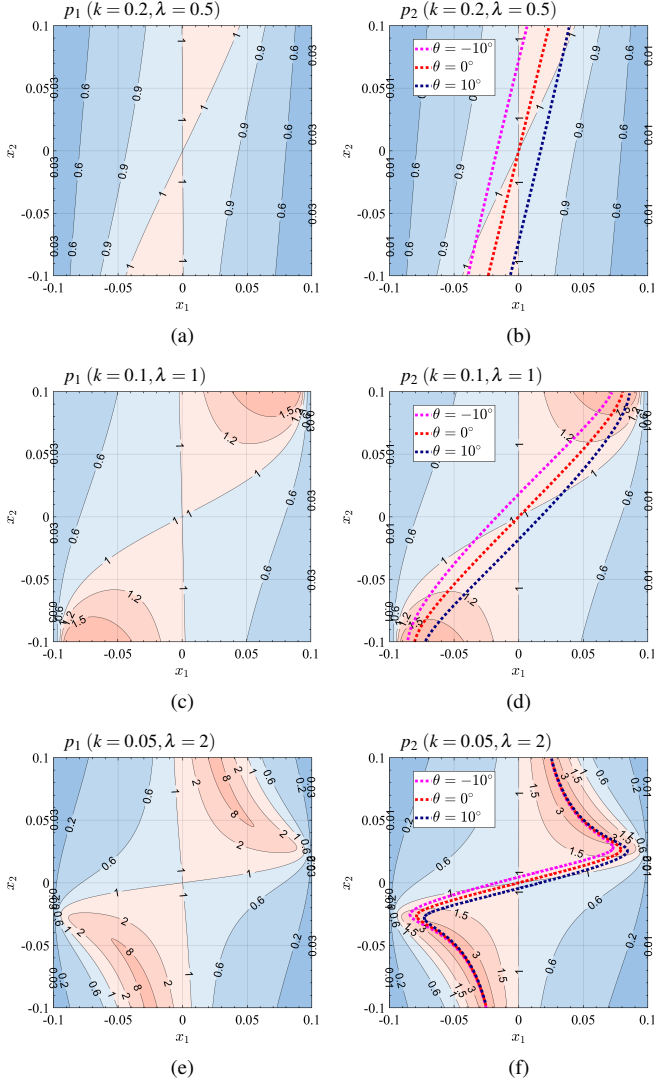


Fig. 3. Colormaps of  $p_1$  and  $p_2$  as functions of  $x_1$  and  $x_2$  under  $q_1 = q_2 = 400$ . (a)  $p_1$  under  $k = 0.2$ ,  $\lambda = 0.5$ . (b)  $p_2$  under  $k = 0.2$ ,  $\lambda = 0.5$ . (c)  $p_1$  under  $k = 0.1$ ,  $\lambda = 1$ . (d)  $p_2$  under  $k = 0.1$ ,  $\lambda = 1$ . (e)  $p_1$  under  $k = 0.05$ ,  $\lambda = 2$ . (f)  $p_2$  under  $k = 0.05$ ,  $\lambda = 2$ .

where

$$\zeta := \frac{\beta + \sqrt{\beta^2 + \alpha\gamma}}{\alpha}, \quad (15)$$

$$\alpha := \lambda^2 k^2 - \frac{1}{q_1^2} - x_1^2, \quad (16)$$

$$\beta := \frac{1}{q_1} \left( \frac{1}{q_1 q_2} + k^2 \right) + \frac{x_1 x_2}{q_2}, \quad (17)$$

$$\gamma := \left( \frac{1}{q_1 q_2} + k^2 - x_1 x_2 \right)^2 + \left( \frac{x_1}{q_2} + \frac{x_2}{q_1} \right)^2. \quad (18)$$

In addition, the phase difference between  $\dot{V}_{1ac}$  and  $\dot{I}_{1ac}$  can be derived as:

$$\theta := \angle \dot{V}_{1ac} - \angle \dot{I}_{1ac} = \arctan \left( \frac{x_1 (\zeta^2 + x_2^2) - x_2 k^2}{\zeta k^2} \right). \quad (19)$$

The detailed derivation of (13)–(19) is given in Appendix A.

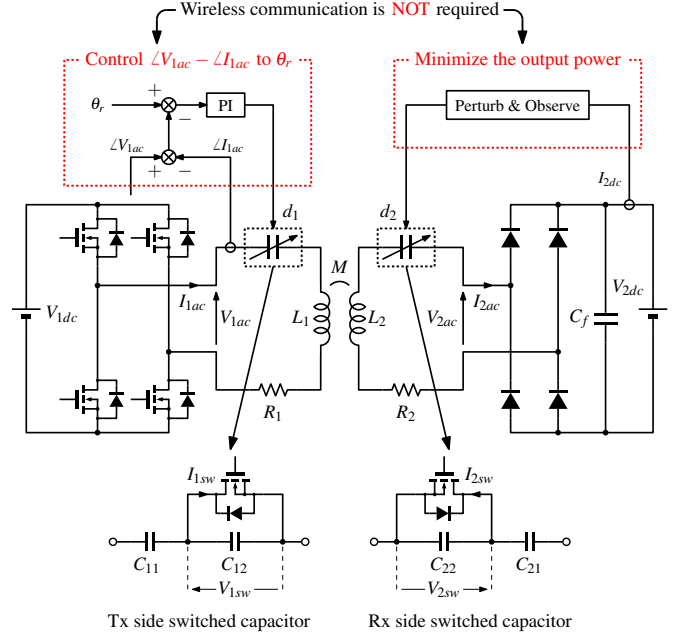


Fig. 4. Overview of the proposed control scheme to maintain the resonance condition and maximize the transmission efficiency.

Fig. 3 shows the colormaps of  $p_1$  and  $p_2$  as functions of  $x_1$  and  $x_2$  under three cases of  $k$  and  $\lambda$ . The colormaps are obtained under  $q_1 = q_2 = 400$ . The contour lines of  $\theta = -10^\circ$ ,  $\theta = 0^\circ$ , and  $\theta = 10^\circ$  are also plotted on the colormaps of  $p_2$ . In all cases, the perfect resonance point *i.e.*  $x_1 = x_2 = 0$  coincides with the minimum point of  $p_2$  on the contour line of  $\theta = 0^\circ$ . In other words, the perfect resonance condition is achieved when the output power is minimized under  $\theta = 0^\circ$ .

The same conclusion can be drawn from a numerical approach. When  $R_1$  and  $R_2$  are sufficiently small, the following approximation can be made:

$$\frac{1}{q_1} \approx 0, \quad \frac{1}{q_2} \approx 0. \quad (20)$$

By substituting (20) and  $\theta = 0^\circ$  into (19), the following relationship between  $x_1$  and  $x_2$  can be derived:

$$x_2 = \frac{1}{\lambda^2} x_1 \quad (21)$$

By substituting (20) and (21) into (14),  $p_2$  can be expressed as a convex downward function under  $\theta = 0^\circ$  as:

$$p_2 = \frac{\lambda k}{\sqrt{\lambda^2 k^2 - x_1^2}} = \frac{k}{\sqrt{k^2 - \lambda^2 x_1^2}} \quad (22)$$

Equation (22) indicates that the minimum point of  $p_2$  under  $\theta = 0^\circ$  is given by  $x_1 = x_2 = 0$ . In other words, the perfect resonance condition is achieved when the output power is minimized under  $\theta = 0^\circ$ . Therefore, the condition for perfect resonance can be expressed as in (4). It should be noted that the proposed condition for perfect resonance is valid for any given coupling coefficient and DC bus voltage ratio.

Based on (4), the variable capacitors can be controlled to maintain the perfect resonance condition without wireless communication.

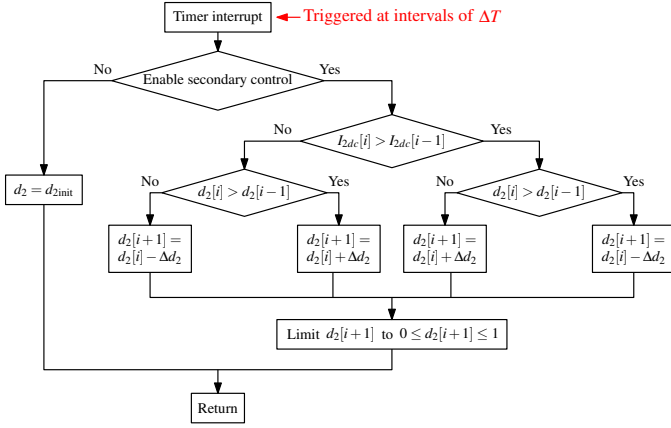


Fig. 5. Flowchart of the P&O algorithm.

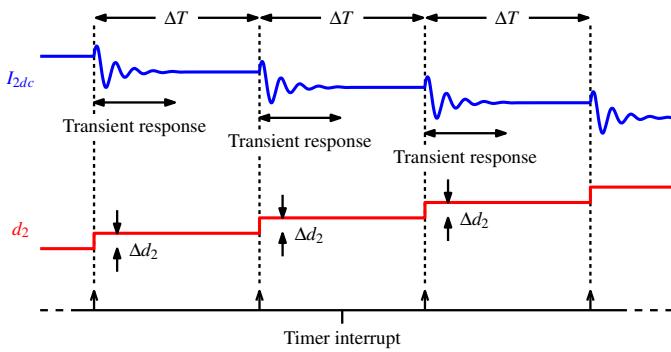


Fig. 6. Timing diagram of the P&O algorithm.

### III. PROPOSED CONTROL SCHEME

#### A. Outline of the Proposed Control Scheme

Based on (4), the perfect resonance condition described in (1)–(4) can be achieved by controlling the variable capacitors as shown in Fig. 4. This control scheme simultaneously performs the following two functions.

- 1) The phase difference between  $V_{1ac}$  and  $I_{1ac}$  is controlled to  $\theta_r = 0^\circ$  by adjusting the Tx side variable capacitor.
- 2) The output power is minimized by adjusting the Rx side variable capacitor.

This control scheme can be explained visually based on the colormap of  $p_2$  in Fig. 3. By controlling the phase difference between  $V_{1ac}$  and  $I_{1ac}$  to  $0^\circ$ ,  $x_1$  and  $x_2$  are constrained to the contour line of  $\theta = 0^\circ$ . Then, by tracking the minimum power point on the contour line of  $\theta = 0^\circ$ ,  $x_1$  and  $x_2$  converge to the perfect resonance point *i.e.*  $x_1 = x_2 = 0$ . As shown in Fig. 4, this control scheme can be implemented by separate closed-loops on the Tx and Rx sides, thus eliminating the need for wireless communication. It should be noted that the exact target values of the variable capacitors do not need to be known in the proposed control scheme. Even if the exact values are not known, the variable capacitors automatically converge to the exact values by simultaneously performing the two functions mentioned above.

In this study, a proportional-integral (PI) controller is adopted for the Tx side control loop, and a perturb and observe (P&O) algorithm [30] is adopted for the Rx side control

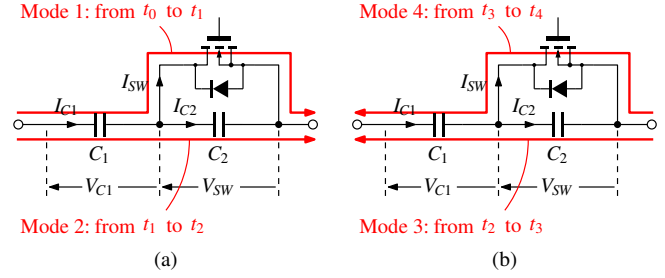


Fig. 7. Current paths of four operational modes of the PWM-controlled switched capacitor. (a) Mode 1 and Mode 2. (b) Mode 3 and Mode 4.

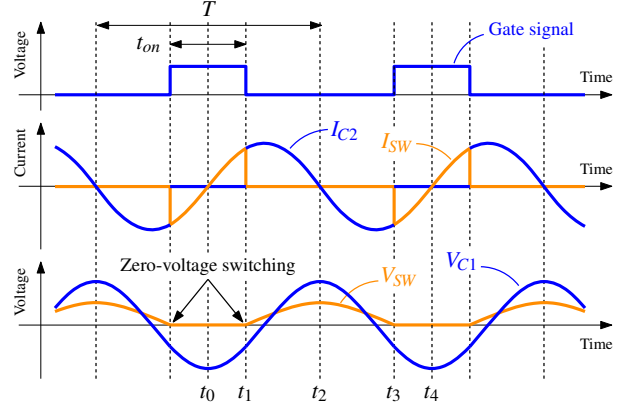


Fig. 8. Key waveforms of the PWM-controlled switched capacitor.

loop. The variable capacitors are realized by PWM-controlled switched capacitors.

#### B. Software Implementation of the Control Scheme

Since  $V_{2dc}$  is constant under the dynamics of the circuit, the output power is proportional to  $I_{2dc}$ . Therefore, as shown in Fig. 5, a P&O algorithm is adopted to search the duty cycle  $d_2$  which yields the minimum  $I_{2dc}$ . The sequence in Fig. 5 is executed at intervals of  $\Delta T$ , and  $d_2$  is increased or decreased by a constant step size of  $\Delta d_2$  in each iteration. Although not depicted in Fig. 5, a digital low-pass filter (LPF) is applied to the value of  $I_{2dc}$  to reduce the noise of the current sensor. The cutoff frequency of the LPF is set to 1 kHz.

A digital PI controller is implemented on the Tx side to regulate the phase difference between  $V_{1ac}$  and  $I_{1ac}$ . In order to avoid conflict between the PI control and the P&O algorithm, the update interval of the P&O algorithm must be designed sufficiently longer than the convergence of the PI control. This condition ensures that the phase difference between  $V_{1ac}$  and  $I_{1ac}$  is regulated to  $0^\circ$  and the circuit is in steady-state when updating  $d_2$  in the P&O algorithm. In other words, this condition ensures that  $x_1$  and  $x_2$  always stay on the contour line of  $\theta = 0^\circ$  in Fig. 3 when minimizing the output power.

As shown in Fig. 6, the transient response of  $I_{2dc}$  occurs immediately after updating  $d_2$ . In order to satisfy the aforementioned condition,  $\Delta T$  must be designed sufficiently longer than the settling time of  $I_{2dc}$ . In this study, the PI gains and the DC link filter capacitor are chosen such that the settling

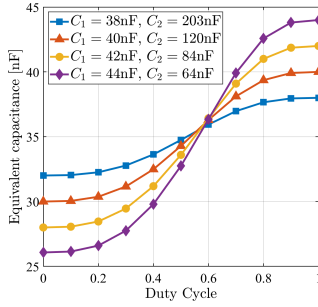


Fig. 9. Equivalent capacitance of the PWM-controlled switched capacitor as a function of the duty cycle.

time is shorter than 1 ms, and  $\Delta T$  is set to 1 ms. Also,  $\Delta d_2$  is set to 0.005.

### C. PWM-Controlled Switched Capacitor

As shown in Fig. 4, the PWM-controlled switched capacitor proposed in [31] and used in [32], [33] is adopted in this study. Compared to the PWM-controlled switched capacitor used in [14], [15], [34], this circuit topology reduces the voltage stress across the switch, thus enabling its use in a wide range of power scales. The voltage stress is reduced since the series connection of the capacitors functions as a voltage divider.

Fig. 7 shows the current paths of four operational modes, and Fig. 8 shows the key waveforms of the switched capacitor. When the switch is always turned ON, the capacitance is equal to  $C_1$ . When the switch is always turned OFF, the capacitance is equal to  $C_1$  and  $C_2$  in series. The equivalent capacitance can take continuous values between the two states by feeding a PWM signal synchronized with the current to the switch. It should be noted that the body diode of the MOSFET is reversely biased in Mode 2 and Mode 3. In fact, the body diode is turned OFF in all operational modes and does not affect the circuit function in terms of the fundamental harmonic. It should also be noted that the switch is turned ON and OFF when  $V_{SW}$  is zero, thus minimizing the switching loss.

By calculating the fundamental harmonic of  $V_{C1} + V_{SW}$ , the equivalent capacitance of the circuit can be derived as:

$$C_{eq} = \frac{1}{\frac{1}{C_1} + \frac{1}{C_2} \left[1 + \frac{1}{2\pi} \sin(2\pi d) - d\right]} \quad (23)$$

where the duty cycle of the gate signal is defined as  $d := t_{on}/T$ . The detailed derivation of (23) is given in Appendix B. Fig. 9 shows the equivalent capacitance as a function of the duty cycle under four cases of  $C_1$  and  $C_2$ . The equivalent capacitance increases non-linearly with the duty cycle. Also, a wider range of capacitance can be achieved by reducing  $C_2$ . However, this increases the impedance of  $C_2$ , thus increasing the voltage stress across the switch. In order to prevent the electrical breakdown of the switch, this trade-off must be considered when determining the values of  $C_1$  and  $C_2$ .

### D. Optimal Condition Considering Inverter Switching Loss

By solving KVL equations derived from Fig. 1 with respect to (5)–(12), the transmission efficiency can be expressed in

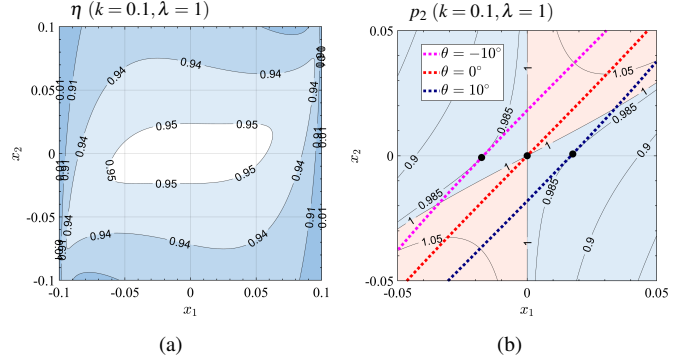


Fig. 10. Colmaps of  $\eta$  and  $p_2$  as functions of  $x_1$  and  $x_2$  under  $q_1 = q_2 = 400$ ,  $k = 0.1$ ,  $\lambda = 1$ . (a) Colormap of  $\eta$ . (b) Close-up colormap of  $p_2$ .

terms of non-dimensional parameters as:

$$\eta = \frac{P_2}{P_1} = \frac{k^2 \zeta}{\frac{x_2^2}{q_1} + \left(\frac{1}{q_2} + \zeta\right) \left(\frac{\zeta}{q_1} + \frac{1}{q_1 q_2} + k^2\right)}. \quad (24)$$

Fig. 10(a) shows the colormap of  $\eta$  as a function of  $x_1$  and  $x_2$  under  $q_1 = q_2 = 400$ ,  $k = 0.1$ ,  $\lambda = 1$ . It is well known that the efficiency does not depend on  $x_1$  when a passive resistor is adopted as the load [16], [21]. However, Fig. 10(a) indicates that  $x_1$  and  $x_2$  both contribute to the decrease in the efficiency when a constant voltage load is adopted. Therefore, it is necessary to compensate for the self-inductance variations of both the Tx and Rx coils to achieve maximum efficiency in practical applications.

It should be noted the perfect resonance condition is not necessarily the optimal condition when considering the end-to-end system efficiency. In fact, the switching loss of the inverter is most reduced when the phase of  $I_{1ac}$  slightly lags the phase of  $V_{1ac}$  [13]. Reducing the switching loss of the inverter is essential to improve the end-to-end system efficiency, as the switching frequency is usually very high (*i.g.* 85 kHz) in WPT applications. Therefore, it is interesting to analyze the behavior of the proposed control scheme when the phase difference between  $V_{1ac}$  and  $I_{1ac}$  is controlled to  $\theta_r \neq 0^\circ$ .

By substituting (20) and  $\theta = \theta_r$  into (19), the relationship between  $x_1$  and  $x_2$  can be derived as:

$$x_2 = \frac{1}{\lambda^2} x_1 - \frac{\tan \theta_r}{\lambda^2} \sqrt{\lambda^2 k^2 - x_1^2} \approx \frac{1}{\lambda^2} x_1 - \frac{k \tan \theta_r}{\lambda}. \quad (25)$$

The right-hand side of (25) is the first-order approximation of  $x_2$  around  $x_1 = 0$ . By substituting (20) and (25) into (14),  $p_2$  can be expressed in terms of  $x_1$ ,  $k$ ,  $\lambda$ , and  $\theta_r$ . Then, the derivative of  $p_2$  with respect to  $x_1$  can be derived in the neighborhood of  $x_1 = 0$  as:

$$\frac{dp_2}{dx_1} \approx \frac{x_1 - \lambda k \tan \theta_r}{(\lambda k + x_1 \tan \theta_r)^2}. \quad (26)$$

Equations (25) and (26) indicate that the minimum point of  $p_2$  under  $\theta = \theta_r$  is given by:

$$x_1 = \lambda k \tan \theta_r, \quad x_2 = 0. \quad (27)$$

In fact,  $x_1$  and  $x_2$  converge to (27) by minimizing the output power under  $\theta = \theta_r$ . It is interesting to point out that the

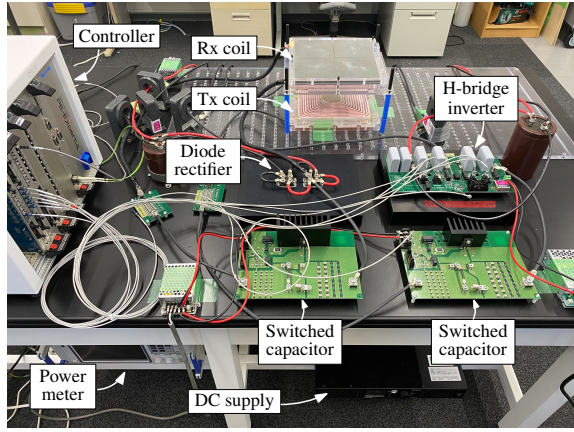


Fig. 11. Experimental setup.

TABLE I  
SPECIFICATIONS OF EXPERIMENTAL SETUP

Description	Symbol	Value	Unit
Operating frequency	-	85.0	kHz
Tx side DC voltage	$V_{1dc}$	100	V
Rx side DC voltage	$V_{2dc}$	100	V
Self-inductance of Tx coil	$L_1$	99.8	$\mu\text{H}$
Self-inductance of Rx coil	$L_2$	101.3	$\mu\text{H}$
Mutual inductance	$M$	14.1	$\mu\text{H}$
ESR of Tx circuit	$R_1$	188	$\text{m}\Omega$
ESR of Rx circuit	$R_2$	202	$\text{m}\Omega$
DC link filter capacitor	$C_f$	470	$\mu\text{F}$
Components of Tx side switched capacitor	$C_{11}$	40.1	nF
	$C_{12}$	149.0	nF
Components of Rx side switched capacitor	$C_{21}$	39.2	nF
	$C_{22}$	148.6	nF

reactance of the Rx circuit can be completely compensated even when the control target of  $\theta$  is set to  $\theta_r \neq 0$ .

The same conclusion can also be confirmed from the close-up colormap of  $p_2$  in Fig. 10(b). The black markers in Fig. 10(b) represent the minimum point of  $p_2$  on the contour lines of  $\theta = -10^\circ$ ,  $\theta = 0^\circ$ , and  $\theta = 10^\circ$ . Moreover, the colormaps of  $p_2$  in Fig. 3 indicate that (27) is the global minimum point of  $p_2$  under  $\theta = \theta_r$ . Therefore, it can be concluded that  $x_1$  and  $x_2$  converge to (27) by minimizing the output power under  $\theta = \theta_r$ .

The optimal  $\theta$  in terms of the switching loss is usually a small positive value within the range from  $0^\circ$  to  $10^\circ$ . Fig. 10 and (27) indicate that when  $\theta_r$  is within this range,  $x_1$  and  $x_2$  converge to the neighborhood of the perfect resonance point where the transmission efficiency is sufficiently high. Therefore, the inverter efficiency can be improved without sacrificing the AC/AC efficiency by adopting a small positive value as  $\theta_r$  in the control scheme.

#### IV. EXPERIMENTAL VERIFICATION

##### A. Experimental Setup

A 1 kW experimental prototype of the proposed system is developed, as shown in Fig. 11. The specifications of the experimental setup are listed in Table. I. The Tx and Rx coils are aligned horizontally, and the vertical gap is fixed

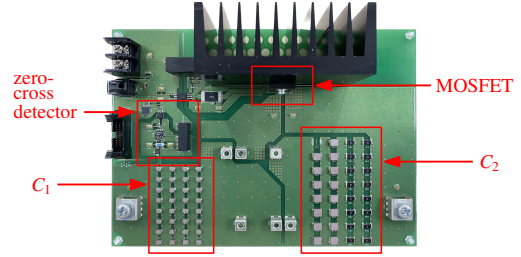


Fig. 12. Prototype board of the PWM-controlled switched capacitor.

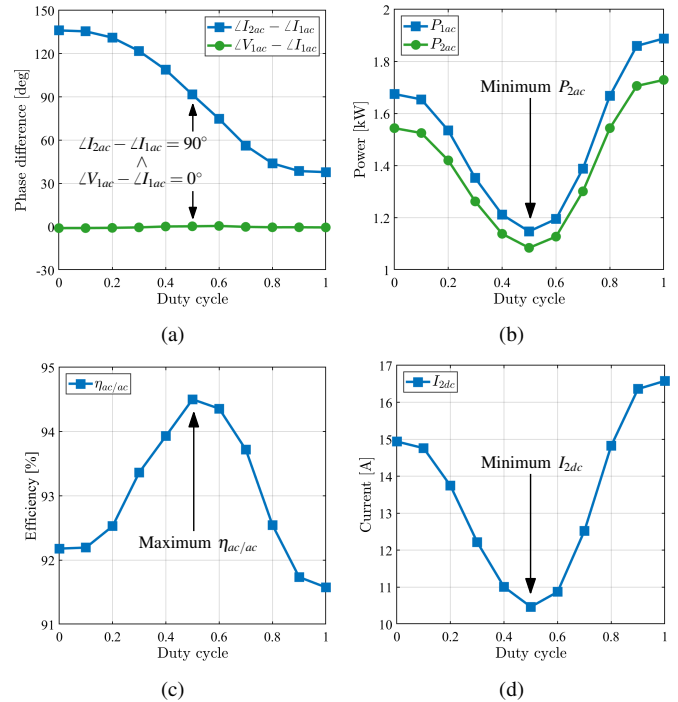


Fig. 13. Steady-state performance of the system according to  $d_2$ . (a) Phase difference between  $I_{1ac}$ ,  $I_{2ac}$ , and  $V_{1ac}$ . (b) Input AC power and output AC power. (c) AC/AC efficiency. (d) Output DC current.

to 100mm. Two prototype boards of the PWM-controlled switched capacitor are fabricated as shown in Fig. 12 and connected to the Tx and Rx circuits. SCT3030KL 1200V/72A SiC MOSFETs are used in the switched capacitor boards. The values of  $C_{11}$ ,  $C_{12}$ ,  $C_{21}$ , and  $C_{22}$  are chosen such that the equivalent capacitance of the switched capacitors vary between 31 to 40 nF. This range is adequate to achieve the perfect resonance condition when the self-inductance of the Tx and Rx coils vary between -10 to +10%. The manufacturing tolerances of electric components are typically larger than  $\pm 5\%$ . Other factors mentioned in Section I cause the self-inductance of the Tx and Rx coils to vary even more. Therefore, in this study, it is assumed that the self-inductance of the Tx and Rx coils vary between -10 to +10%. Moreover, the values of  $C_{11}$ ,  $C_{12}$ ,  $C_{21}$ , and  $C_{22}$  guarantee that the voltage stress across the MOSFET is sufficiently lower than 1200V when achieving an output power of 1 kW. In the experimental results, the power and efficiency are measured using HIOKI PW6001, and the phase difference is obtained by applying fast Fourier transforms to the waveforms of the oscilloscope.

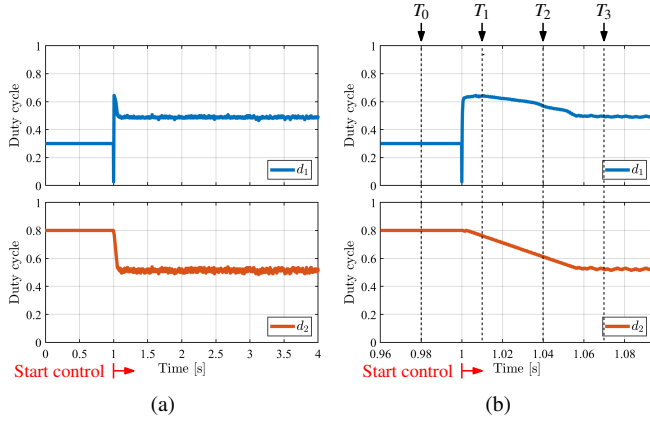


Fig. 14. Trajectories of  $d_1$  and  $d_2$  when applying the proposed control scheme, shown in two different time scales. (a) 0.5s/div. (b) 0.02s/div.

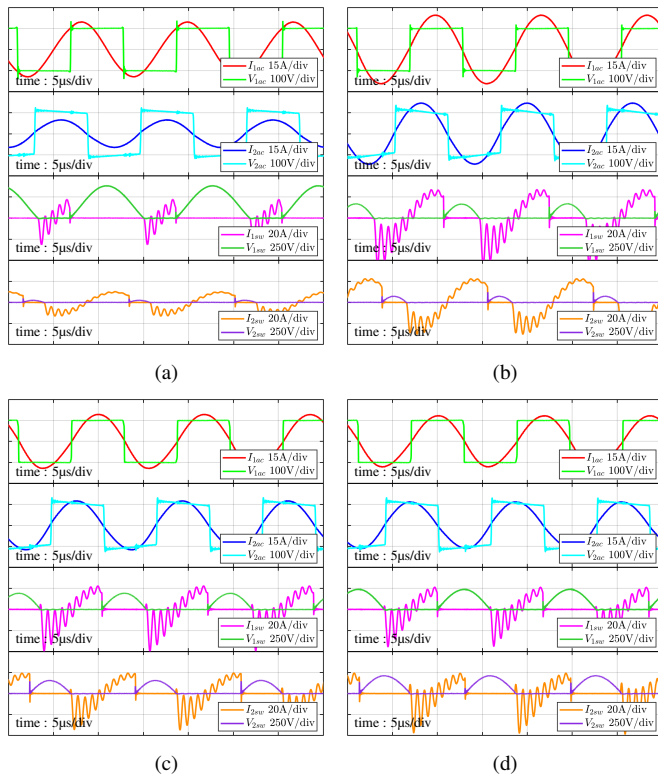


Fig. 15. Waveforms of  $I_{1ac}$ ,  $V_{1ac}$ ,  $I_{2ac}$ ,  $V_{2ac}$ ,  $I_{1sw}$ ,  $V_{1sw}$ ,  $I_{2sw}$ , and  $V_{2sw}$  at (a)  $t = T_0$ , (b)  $t = T_1$ , (c)  $t = T_2$ , and (d)  $t = T_3$ .

### B. Verification of the Theoretical Analysis

In order to verify the condition for perfect resonance derived in Section II-B, the following experiment is conducted. On the primary side, the phase difference between  $V_{1ac}$  and  $I_{1ac}$  is regulated to  $0^\circ$  by the PI controller. On the secondary side, the duty cycle of the switched capacitor,  $d_2$  is varied in increments of 0.1 between 0 and 1. It should be noted that the P&O algorithm is not applied in this experiment.

Fig. 13 shows the experimental results. The phase difference between  $I_{1ac}$  and  $I_{2ac}$  is approximately  $90^\circ$  at  $d_2 = 0.5$ . This means that the perfect resonance condition described in (3) is satisfied at  $d_2 = 0.5$ . Also, the output AC power is minimum, and the AC/AC efficiency is maximum at  $d_2 = 0.5$ . In fact, the

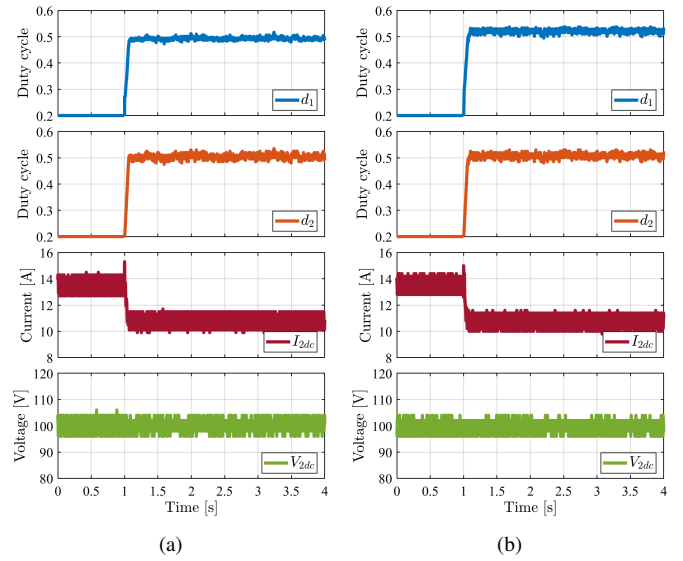


Fig. 16. Trajectories of  $d_1$ ,  $d_2$  and waveforms of  $I_{2dc}$ ,  $V_{2dc}$  when applying the proposed control scheme with (a)  $\theta_r = 0^\circ$  and (b)  $\theta_r = 5^\circ$ .

TABLE II  
STEADY-STATE PERFORMANCE OF THE PROPOSED SYSTEM

	$\angle V_{1ac} - \angle I_{1ac}$	$\angle I_{2ac} - \angle I_{1ac}$	$\eta_{inv}$	$\eta_{ac/ac}$	$\eta_{dc/dc}$	$P_{2ac}$
$\theta_r = 0^\circ$	$0.5^\circ$	$89.9^\circ$	98.0%	94.5%	90.4%	1.1 kW
$\theta_r = 5^\circ$	$4.8^\circ$	$90.2^\circ$	98.8%	94.5%	90.8%	1.1 kW

perfect resonance point coincides with the minimum output power point when  $\angle V_{1ac} - \angle I_{1ac}$  is regulated to  $0^\circ$ . These results verify the condition for perfect resonance shown in (4). In addition, Fig. 13(d) implies that the perfect resonance point can be reached by minimizing  $I_{2dc}$  instead of  $P_{2ac}$ .

Fig. 14 shows the trajectories of  $d_1$  and  $d_2$  when the PI control and the P&O algorithm are both applied. The initial values of  $d_1$  and  $d_2$  are set to 0.3 and 0.8. The step size of  $d_2$  in the P&O algorithm is set to 0.005 as described in Section III-B.  $\theta_r$  is set to  $0^\circ$ . In addition, Fig. 15 shows the voltage and current waveforms measured at four points  $T_0, T_1, T_2, T_3$  in Fig. 14(b). The working principle of the proposed control scheme can be explained step by step as follows.

$t = T_0$ :  $d_1$  and  $d_2$  are fixed to their initial values before the control starts.  $V_{1ac}$  and  $I_{1ac}$  are out of phase, and the phase difference between  $I_{1ac}$  and  $I_{2ac}$  is less than  $90^\circ$ .

$t = T_1$ : The phase difference between  $V_{1ac}$  and  $I_{1ac}$  is regulated to  $0^\circ$  by the PI controller. However, the phase difference between  $I_{1ac}$  and  $I_{2ac}$  is still less than  $90^\circ$ , since the convergence of the P&O algorithm is slow compared to the PI control as described in Section III-B.

$t = T_2$ : The phase difference between  $V_{1ac}$  and  $I_{1ac}$  is maintained to  $0^\circ$  while the phase difference between  $I_{1ac}$  and  $I_{2ac}$  is approaching  $90^\circ$ . This corresponds to the output power being minimized on the contour line of  $\theta = 0^\circ$  in Fig. 3.

$t = T_3$ : The P&O algorithm reaches convergence and the perfect resonance condition is achieved.  $V_{1ac}$  and  $I_{1ac}$  are in phase, and the phase difference between  $I_{1ac}$  and  $I_{2ac}$  is  $90^\circ$ .

Fig. 16 and Table II show the comparison of applying the



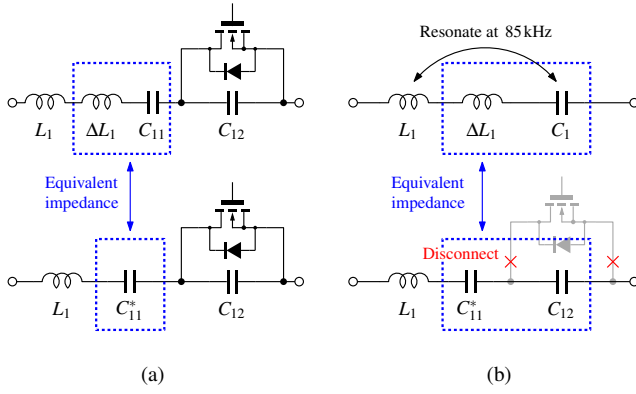


Fig. 17. Modification of  $C_{11}$  to emulate the self-inductance variation of the Tx coil connected to (a) a switched capacitor and (b) a passive capacitor.

TABLE III  
MODIFIED VALUES OF THE SERIES-CONNECTED CAPACITORS

Case	$\Delta L_1$	$\Delta L_2$	$C_{11}^*$	$C_{21}^*$	Capacitor type
A-1	+10 $\mu\text{H}$	+10 $\mu\text{H}$	45.07 nF	44.22 nF	Switched
A-2	+10 $\mu\text{H}$	-10 $\mu\text{H}$	45.07 nF	35.25 nF	Switched
A-3	-10 $\mu\text{H}$	+10 $\mu\text{H}$	35.68 nF	44.22 nF	Switched
A-4	-10 $\mu\text{H}$	-10 $\mu\text{H}$	35.68 nF	35.25 nF	Switched
B-1	+10 $\mu\text{H}$	+10 $\mu\text{H}$	53.34 nF	52.17 nF	Passive
B-2	+10 $\mu\text{H}$	-10 $\mu\text{H}$	53.34 nF	40.22 nF	Passive
B-3	-10 $\mu\text{H}$	+10 $\mu\text{H}$	40.87 nF	52.17 nF	Passive
B-4	-10 $\mu\text{H}$	-10 $\mu\text{H}$	40.87 nF	40.22 nF	Passive

proposed control scheme with  $\theta_r = 0^\circ$  and  $\theta_r = 5^\circ$ . The initial values of  $d_1$  and  $d_2$  are set to 0.2.  $\eta_{inv}$ ,  $\eta_{ac/ac}$ , and  $\eta_{dc/dc}$  represent the inverter efficiency, the AC/AC efficiency, and the DC/DC efficiency, respectively. As shown in Fig. 16(b), when  $\angle V_{1ac} - \angle I_{1ac}$  is regulated to  $5^\circ$ ,  $d_1$  converges to a stable value slightly higher than in Fig. 16(a). This indicates that the equivalent capacitance of the Tx side switched capacitor is increased such that the impedance of the circuit becomes slightly inductive. As shown in Table II,  $\angle I_{2ac} - \angle I_{1ac}$  converges to approximately  $90^\circ$  in both cases of  $\theta_r = 0^\circ$  and  $\theta_r = 5^\circ$ . However, the latter case achieves a higher DC/DC efficiency, since the inverter efficiency is higher by 0.8% compared to the former case. These results verify the effectiveness of adopting a small positive value as  $\theta_r$  in the proposed control scheme. It can also be seen from Fig. 16 that  $I_{2dc}$  settles to a stable value around 11 A, thus verifying the stability of the system output.

### C. Assessment Under Diverse Patterns of Self-Inductance Variations

In order to verify the versatility of the proposed control scheme, its performance is tested against diverse patterns of self-inductance variations. Instead of directly changing the self-inductance of the coils, the values of  $C_{11}$  and  $C_{21}$  are modified to obtain the equivalent impedance, as shown in Fig. 17(a).  $\Delta L_1$  represents the self-inductance variation of the Tx coil, and  $C_{11}^*$  represents the modified value of  $C_{11}$ .

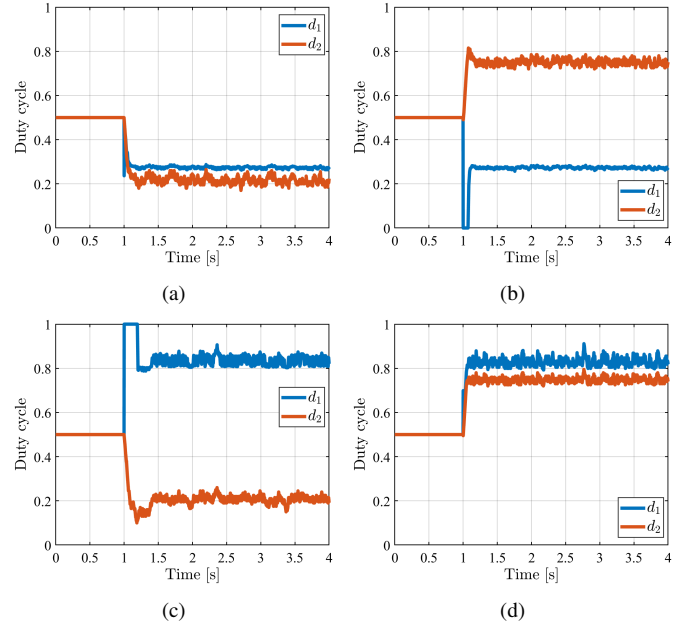


Fig. 18. Trajectories of  $d_1$  and  $d_2$  under the four cases of self-inductance variations. (a) Case A-1. (b) Case A-2. (c) Case A-3. (d) Case A-4.

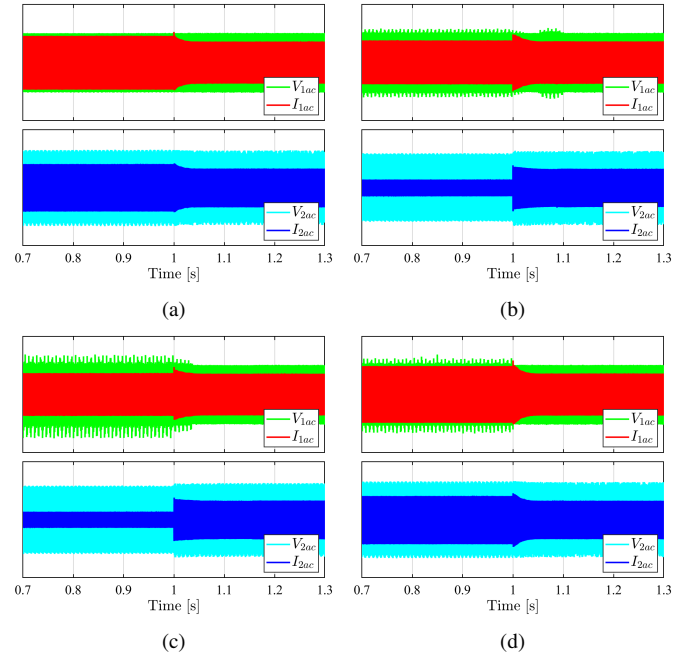


Fig. 19. Transient response of  $I_{1ac}$ ,  $V_{1ac}$ ,  $I_{2ac}$ , and  $V_{2ac}$ . (a) Case A-1. (b) Case A-2. (c) Case A-3. (d) Case A-4.

In the experiment, the performance of the proposed control scheme is compared with cases in which passive capacitors are adopted instead of switched capacitors. The passive capacitors are realized by disconnecting the MOSFETs from the switched capacitor circuits and modifying the values of  $C_{11}$  and  $C_{21}$ , as shown in Fig. 17(b). Table III lists the values of  $C_{11}^*$  and  $C_{21}^*$  corresponding to the four cases of self-inductance variations. Case A-1, A-2, ... are the cases in which switched capacitors are adopted, as shown in Fig. 17(a). Case B-1, B-2, ... are the cases in which passive capacitors are adopted, as shown

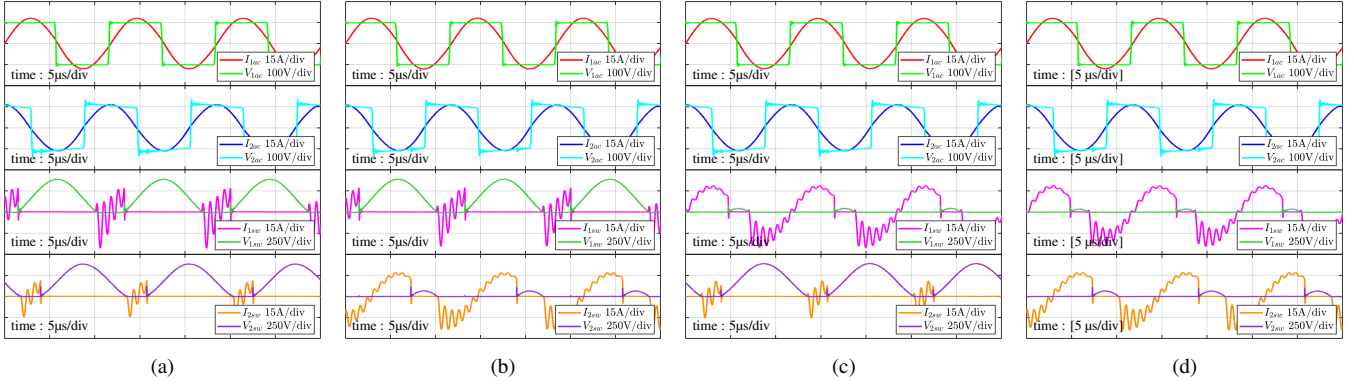


Fig. 20. Waveforms of  $I_{1ac}$ ,  $V_{1ac}$ ,  $I_{2ac}$ ,  $V_{2ac}$ ,  $I_{1sw}$ ,  $V_{1sw}$ ,  $I_{2sw}$ , and  $V_{2sw}$  after convergence in (a) Case A-1, (b) Case A-2, (c) Case A-3, and (d) Case A-4.

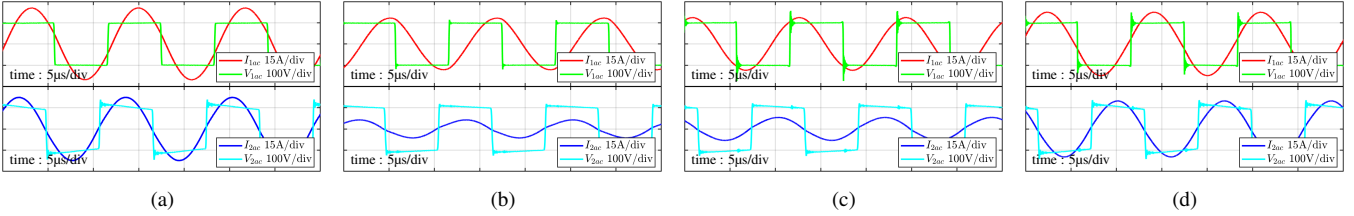


Fig. 21. Waveforms of  $I_{1ac}$ ,  $V_{1ac}$ ,  $I_{2ac}$ , and  $V_{2ac}$  in (a) Case B-1, (b) Case B-2, (c) Case B-3, and (d) Case B-4.

TABLE IV  
PHASE DIFFERENCE MEASURED AT STEADY-STATE

Case	$\angle V_{1ac} - \angle I_{1ac}$	$\angle I_{2ac} - \angle I_{1ac}$	Case	$\angle V_{1ac} - \angle I_{1ac}$	$\angle I_{2ac} - \angle I_{1ac}$
A-1	5.09°	90.84°	B-1	13.83°	45.16°
A-2	4.95°	90.46°	B-2	67.93°	104.91°
A-3	5.08°	91.56°	B-3	-60.68°	71.90°
A-4	4.76°	89.89°	B-4	-11.25°	125.35°

in Fig. 17(b). In the experiment,  $\theta_r$  is set to  $5^\circ$ . The initial values of  $d_1$  and  $d_2$  are set to 0.5.

Fig. 18 shows the trajectories of  $d_1$  and  $d_2$ , and Fig. 19 shows the transient response of  $I_{1ac}$ ,  $V_{1ac}$ ,  $I_{2ac}$ , and  $V_{2ac}$  in Case A-1, A-2, A-3, and A-4. Fig. 20 and Fig. 21 show the voltage and current waveforms measured at steady-state in the eight cases listed in Table III. Table IV summarizes the phase difference between  $V_{1ac}$ ,  $I_{1ac}$ , and  $I_{2ac}$  in Fig. 20 and Fig. 21. As shown in Fig. 18(b),  $d_1$  converges to  $\sim 0.27$ , and  $d_2$  converges to  $\sim 0.75$  in Case A-2. Compared to Fig. 16(b),  $d_1$  is decreased to compensate for the increase in the Tx coil's self-inductance, while  $d_2$  is increased to compensate for the decrease in the Rx coil's self-inductance. Similarly, the behaviors of  $d_1$  and  $d_2$  in Fig. 18(a), (c), and (d) all reflect the values of  $\Delta L_1$  and  $\Delta L_2$  listed in Table III. The waveforms in Fig. 19 indicate that  $I_{1ac}$ ,  $V_{1ac}$ ,  $I_{2ac}$ , and  $V_{2ac}$  are stabilized in less than 100 ms after the control starts. As shown in Fig. 20 and Table IV,  $\angle V_{1ac} - \angle I_{1ac}$  converges to approximately  $5^\circ$ , and  $\angle I_{2ac} - \angle I_{1ac}$  converges to approximately  $90^\circ$  in Case A-1, A-2, A-3, and A-4. On the other hand, as shown in Fig. 21 and Table IV, the phase difference between  $\angle V_{1ac}$ ,  $\angle I_{1ac}$ , and  $\angle I_{2ac}$  are far from optimal in Case B-1, B-2, B-3, and

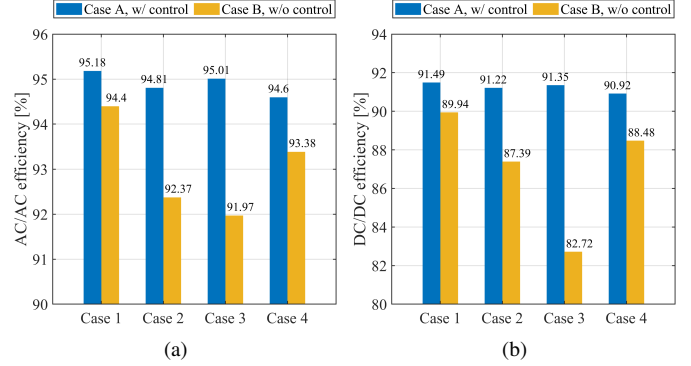


Fig. 22. (a) AC/AC efficiency and (b) DC/DC efficiency measured at steady-state under the four cases of self-inductance variations.

B-4. These results show that the proposed control scheme can flexibly adapt to diverse patterns of self-inductance variations and maintain the resonance condition.

As shown in Fig. 20, small vibrations appear in the waveforms of  $I_{1sw}$  and  $I_{2sw}$  immediately after the MOSFET turns ON. These vibrations are caused by the parasitic inductance in the switched capacitor board. However, the overall system performance is unaffected, since the vibrations occur locally within the switched capacitor circuit. Moreover, the peak values of  $V_{1sw}$  and  $V_{2sw}$  are sufficiently lower than the MOSFET voltage rating. These waveforms verify the functionality of the PWM-controlled switched capacitor.

Fig. 22 (a) and (b) show the AC/AC efficiency and DC/DC efficiency in the eight cases listed in Table III, all of which are measured at steady-state. When passive capacitors are adopted (*i.e.* Case B-1, B-2, ...), the AC/AC efficiency and DC/DC efficiency vary significantly depending on the self-

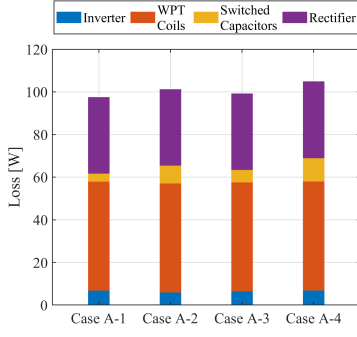


Fig. 23. Loss distribution measured at steady-state when the proposed control scheme is applied against the four cases of self-inductance variations.

inductance variations. On the other hand, when the proposed control scheme is applied (*i.e.* Case A-1, A-2, ...), the system maintains a stable AC/AC efficiency and DC/DC efficiency regardless of the self-inductance variations. The comparison of Case A-2 and B-2 indicates that the AC/AC efficiency and DC/DC efficiency are increased by 3.59% and 4.98%, respectively, by applying the proposed control scheme under  $\Delta L_1 = +10 \mu\text{H}$ ,  $\Delta L_2 = -10 \mu\text{H}$ . The AC/AC efficiency is increased since the system operates near the perfect resonance point by applying the proposed control scheme. The additional increase in the DC/DC efficiency results from the reduction in the switching loss of the inverter. The same argument can be applied to the other three cases of self-inductance variations. These results verify that the proposed system can maintain a high end-to-end system efficiency by flexibly adapting to the self-inductance variations of the Tx and Rx coils.

Fig. 23 shows the loss distribution of the system measured at steady-state in Case A-1, A-2, A-3, and A-4. Since it is difficult to directly measure the loss of the switched capacitors, the loss of the switched capacitors is estimated by subtracting the AC loss of the circuit with optimal passive capacitors from the AC loss of the circuit with switched capacitors. The loss of the inverter, the WPT coils, and the rectifier are roughly the same among the four cases. On the other hand, there is a noticeable difference in the loss of the switched capacitors. The main reason for this is the difference in the conduction time of the MOSFETs. As shown in Fig. 18, the final values of  $d_1$  and  $d_2$  in Case A-4 are the highest among the four cases, resulting in the longest conduction time of the MOSFETs. However, in either case, the loss of the switched capacitors is sufficiently small compared to the loss of the WPT coils, indicating that the switched capacitors have only minor negative effects on the system efficiency.

## V. CONCLUSION

In this paper, a control scheme for PWM-controlled switched capacitors was proposed to compensate for the self-inductance variations of the Tx and Rx coils without wireless communication. The novelty of this paper is a unique condition for perfect resonance which was derived by focusing on the output power of the WPT circuit. Based on this condition, the switched capacitors can be controlled simultaneously by separate closed-loops on the Tx and Rx sides, thus eliminat-

ing the need for wireless communication. The condition for perfect resonance was experimentally verified using a 1-kW prototype of the proposed system. The experimental results also revealed that the switched capacitors can flexibly adapt to diverse patterns of self-inductance variations and maintain the resonance condition. The AC/AC efficiency and DC/DC efficiency were both improved compared to the cases in which passive capacitors were adopted.

The condition for perfect resonance and the basic concept of the control scheme can generally be applied to any S-S compensated WPT system interfacing constant voltage DC buses. It should be noted that the optimal charging process of batteries *i.e.* constant current (CC) and constant voltage (CV) charging [22], [34] was not considered in this paper. The integration of the proposed control scheme with CC and CV charging is an important topic for future research. Other future works include the investigation of variable capacitor circuits applicable to higher power levels and the optimization of control parameters to improve the response speed.

## APPENDIX A

By applying Kirchhoff's voltage law to the circuit in Fig. 1, the following equations can be obtained:

$$\dot{V}_{1ac} = \left( j\omega L_1 + \frac{1}{j\omega C_1} + R_1 \right) \dot{I}_{1ac} - j\omega M \dot{I}_{2ac}, \quad (\text{A1})$$

$$\dot{V}_{2ac} = j\omega M \dot{I}_{1ac} - \left( j\omega L_2 + \frac{1}{j\omega C_2} + R_2 \right) \dot{I}_{2ac}. \quad (\text{A2})$$

The equivalent load resistance of the circuit is defined as:

$$R_L := \frac{\dot{V}_{2ac}}{\dot{I}_{2ac}}. \quad (\text{A3})$$

It should be noted that when  $V_{2dc}$  is constant,  $R_L$  is not constant and can vary depending on other circuit parameters such as  $X_1$ ,  $X_2$ , and  $M$ . This causes a significant difference in the circuit characteristics when compared to modeling the load as a passive resistor. By substituting (A3) into (A1) and (A2),  $R_L$  can be expressed in terms of the constants defined in Fig. 1, Fig. 2, and (7) as:

$$R_L = \frac{B + \sqrt{B^2 + AC}}{A} \quad (\text{A4})$$

where

$$A := \frac{V_{1dc}^2}{V_{2dc}^2} (\omega M)^2 - R_1^2 - X_1^2, \quad (\text{A5})$$

$$B := R_1 [R_1 R_2 + (\omega M)^2] + R_2 X_1 X_2, \quad (\text{A6})$$

$$C := [R_1 R_2 + (\omega M)^2 - X_1 X_2]^2 + (R_1 X_2 + R_2 X_1)^2. \quad (\text{A7})$$

The input power and the output power can be expressed using  $R_L$  as:

$$P_1 = R_1 |\dot{I}_{1ac}|^2 + R_2 |\dot{I}_{2ac}|^2 + \frac{|\dot{V}_{2ac}|^2}{R_L}, \quad (\text{A8})$$

$$P_2 = \frac{|\dot{V}_{2ac}|^2}{R_L}. \quad (\text{A9})$$

From (A1)–(A3),  $P_1$  can be rewritten as:

$$P_1 = \left[ \frac{X_2^2 + (R_2 + R_L)^2}{R_L^2 (\omega M)^2} R_1 + \frac{R_2}{R_L^2} + \frac{1}{R_L} \right] |\dot{V}_{2ac}|^2. \quad (\text{A10})$$

By substituting (A4)–(A7) into (A9) and (A10),  $P_1$  and  $P_2$  can be expressed without using  $R_L$ . Finally, the per-unit expressions of  $P_1$  and  $P_2$  can be derived using the definitions in (8)–(12) as in (13) and (14).

The impedance at the input of the circuit in Fig. 1 can be expressed using  $R_L$  as:

$$Z_{in} = \frac{R_L (\omega M)^2}{R_L^2 + X_2^2} + j \left[ X_1 - \frac{X_2 (\omega M)^2}{R_L^2 + X_2^2} \right]. \quad (\text{A11})$$

Therefore, the phase difference between  $\dot{V}_{1ac}$  and  $\dot{I}_{1ac}$  can be expressed using the definitions in (8)–(12) as:

$$\theta = \arctan \left( \frac{\text{Im} [Z_{in}]}{\text{Re} [Z_{in}]} \right) = \arctan \left( \frac{x_1 (\zeta^2 + x_2^2) - x_2 k^2}{\zeta k^2} \right). \quad (\text{A12})$$

## APPENDIX B

Due to the bandpass characteristic of the resonant network,  $I_{C1}$  in Fig. 7 can be approximated as a sine wave as:

$$I_{C1} = A \sin \left( \frac{2\pi}{T} t \right) \quad (\text{B1})$$

where  $A$  is the amplitude and  $T$  is the period of  $I_{C1}$ . Therefore,  $V_{C1}$  can be expressed as:

$$V_{C1} = -\frac{AT}{2\pi C_1} \cos \left( \frac{2\pi}{T} t \right) \quad (\text{B2})$$

and  $V_{SW}$  can be expressed as:

$$V_{SW} = \begin{cases} 0 & : \text{in Mode 1 and Mode 4} \\ \frac{1}{C_2} \int_{t_1}^t I_{C1} dt & : \text{in Mode 2 and Mode 3} \end{cases} \quad (\text{B3})$$

From (B1)–(B3), the fundamental harmonic of  $V_{C1} + V_{SW}$  can be derived by Fourier series expansion:

$$\begin{aligned} V_{fh} &= \frac{2}{T} \int_{t_0}^{t_4} (V_{C1} + V_{SW}) \cos \left( \frac{2\pi}{T} t \right) dt \\ &= -\frac{AT}{2\pi} \left\{ \frac{1}{C_1} + \frac{1}{C_2} \left[ 1 + \frac{1}{2\pi} \sin(2\pi d) - d \right] \right\} \end{aligned} \quad (\text{B4})$$

where  $d$  is the duty cycle of the PWM signal. Therefore, the equivalent capacitance of the switched capacitor circuit can be expressed in terms of  $d$  as:

$$C_{eq} = -\frac{A}{V_{fh}} \times \frac{T}{2\pi} = \frac{1}{\frac{1}{C_1} + \frac{1}{C_2} \left[ 1 + \frac{1}{2\pi} \sin(2\pi d) - d \right]}. \quad (\text{B5})$$

## REFERENCES

- [1] Y. Jang and M. Jovanovic, "A contactless electrical energy transmission system for portable-telephone battery chargers," *IEEE Trans. Ind. Electron.*, vol. 50, no. 3, pp. 520–527, 2003.
- [2] M. Sato, G. Yamamoto, D. Gunji, T. Imura, and H. Fujimoto, "Development of wireless in-wheel motor using magnetic resonance coupling," *IEEE Trans. Power Electron.*, vol. 31, no. 7, pp. 5270–5278, 2016.
- [3] A. Kurs, A. Karalis, R. Moffatt, J. D. Joannopoulos, P. Fisher, and M. Soljačić, "Wireless power transfer via strongly coupled magnetic resonances," *Science*, vol. 317, no. 5834, pp. 83–86, 2007.
- [4] T. Imura and Y. Hori, "Maximizing air gap and efficiency of magnetic resonant coupling for wireless power transfer using equivalent circuit and neumann formula," *IEEE Trans. Ind. Electron.*, vol. 58, no. 10, pp. 4746–4752, 2011.
- [5] W. Zhang and C. C. Mi, "Compensation topologies of high-power wireless power transfer systems," *IEEE Trans. Veh. Technol.*, vol. 65, no. 6, pp. 4768–4778, 2016.
- [6] "Wireless power transfer for light-duty plug-in/electric vehicles and alignment methodology," SAE International, 2022.
- [7] S. Y. Jeong, J. H. Park, G. P. Hong, and C. T. Rim, "Autotuning control system by variation of self-inductance for dynamic wireless ev charging with small air gap," *IEEE Trans. Power Electron.*, vol. 34, no. 6, pp. 5165–5174, 2019.
- [8] S. Y. Jeong, V. X. Thai, J. H. Park, and C. T. Rim, "Self-inductance-based metal object detection with mistuned resonant circuits and nullifying induced voltage for wireless ev chargers," *IEEE Trans. Power Electron.*, vol. 34, no. 1, pp. 748–758, 2019.
- [9] J. Lu, G. Zhu, and C. C. Mi, "Foreign object detection in wireless power transfer systems," *IEEE Trans. Ind. Appl.*, vol. 58, no. 1, pp. 1340–1354, 2022.
- [10] G. A. Covic, J. Boys, A. Tam, and J. C.-H. Peng, "Self tuning pickups for inductive power transfer," in *Proc. IEEE Power Electron. Spec. Conf.*, 2008, pp. 3489–3494.
- [11] T. C. Beh, M. Kato, T. Imura, S. Oh, and Y. Hori, "Automated impedance matching system for robust wireless power transfer via magnetic resonance coupling," *IEEE Trans. Ind. Electron.*, vol. 60, no. 9, pp. 3689–3698, 2013.
- [12] Y. Lim, H. Tang, S. Lim, and J. Park, "An adaptive impedance-matching network based on a novel capacitor matrix for wireless power transfer," *IEEE Trans. Power Electron.*, vol. 29, no. 8, pp. 4403–4413, 2014.
- [13] J. Osawa, T. Isobe, and H. Tadano, "Efficiency improvement of high frequency inverter for wireless power transfer system using a series reactive power compensator," in *Proc. IEEE 12th Int. Conf. Power Electron. Drive Syst.*, 2017, pp. 992–998.
- [14] D.-H. Kim and D. Ahn, "Self-tuning lcc inverter using pwm-controlled switched capacitor for inductive wireless power transfer," *IEEE Trans. Ind. Electron.*, vol. 66, no. 5, pp. 3983–3992, 2019.
- [15] H. Zhang, Y. Chen, C.-H. Jo, S.-J. Park, and D.-H. Kim, "Dc-link and switched capacitor control for varying coupling conditions in inductive power transfer system for unmanned aerial vehicles," *IEEE Trans. Power Electron.*, vol. 36, no. 5, pp. 5108–5120, 2021.
- [16] J. Zhang, J. Zhao, Y. Zhang, and F. Deng, "A wireless power transfer system with dual switch-controlled capacitors for efficiency optimization," *IEEE Trans. Power Electron.*, vol. 35, no. 6, pp. 6091–6101, 2020.
- [17] W. Li, G. Wei, C. Cui, X. Zhang, and Q. Zhang, "A double-side self-tuning lcc/s system using a variable switched capacitor based on parameter recognition," *IEEE Trans. Ind. Electron.*, vol. 68, no. 4, pp. 3069–3078, 2021.
- [18] W. Li, Q. Zhang, C. Cui, and G. Wei, "A self-tuning s/s compensation wpt system without parameter recognition," *IEEE Trans. Ind. Electron.*, vol. 69, no. 7, pp. 6741–6750, 2022.
- [19] A. Berger, M. Agostinelli, S. Vesti, J. A. Oliver, J. A. Cobos, and M. Huemer, "A wireless charging system applying phase-shift and amplitude control to maximize efficiency and extractable power," *IEEE Trans. Power Electron.*, vol. 30, no. 11, pp. 6338–6348, 2015.
- [20] K. Colak, E. Asa, M. Bojarski, D. Czarkowski, and O. C. Onar, "A novel phase-shift control of semibridgeless active rectifier for wireless power transfer," *IEEE Trans. Power Electron.*, vol. 30, no. 11, pp. 6288–6297, 2015.
- [21] R. Mai, Y. Liu, Y. Li, P. Yue, G. Cao, and Z. He, "An active-rectifier-based maximum efficiency tracking method using an additional measurement coil for wireless power transfer," *IEEE Trans. Power Electron.*, vol. 33, no. 1, pp. 716–728, 2018.
- [22] S. Ann and B. K. Lee, "Analysis of impedance tuning control and synchronous switching technique for a semibridgeless active rectifier

- in inductive power transfer systems for electric vehicles," *IEEE Trans. Power Electron.*, vol. 36, no. 8, pp. 8786–8798, 2021.
- [23] M. Ishihara, K. Fujiki, K. Umetani, and E. Hiraki, "Autonomous system concept of multiple-receiver inductive coupling wireless power transfer for output power stabilization against cross-interference among receivers and resonance frequency tolerance," *IEEE Trans. Ind. Appl.*, vol. 57, no. 4, pp. 3898–3910, 2021.
- [24] X. Xie, C. Xie, Y. Li, J. Wang, Y. Du, and L. Li, "Adaptive decoupling between receivers of multireceiver wireless power transfer system using variable switched capacitor," *IEEE Trans. Transport. Electrific.*, vol. 7, no. 4, pp. 2143–2155, 2021.
- [25] R. Matsumoto and H. Fujimoto, "Adaptive compensation scheme for wireless power transfer systems with coil inductance variation using pwm-controlled switched capacitor," in *2022 Wireless Power Week (WPW)*, 2022, pp. 244–248.
- [26] Z. Ma, M. Xiao, Y. Xiao, Z. Pang, H. V. Poor, and B. Vucetic, "High-reliability and low-latency wireless communication for internet of things: Challenges, fundamentals, and enabling technologies," *IEEE Internet Things J.*, vol. 6, no. 5, pp. 7946–7970, 2019.
- [27] D. Patil, M. K. McDonough, J. M. Miller, B. Fahimi, and P. T. Balsara, "Wireless power transfer for vehicular applications: Overview and challenges," *IEEE Trans. Transport. Electrific.*, vol. 4, no. 1, pp. 3–37, 2018.
- [28] G. Guidi and J. A. Suul, "Minimizing converter requirements of inductive power transfer systems with constant voltage load and variable coupling conditions," *IEEE Trans. Ind. Electron.*, vol. 63, no. 11, pp. 6835–6844, 2016.
- [29] J. Zhou, G. Guidi, K. Ljøkelsøy, and J. A. Suul, "Evaluation and suppression of oscillations in inductive power transfer systems with constant voltage load and pulse skipping modulation," *IEEE Trans. Power Electron.*, pp. 1–14, 2023.
- [30] N. Femia, G. Petrone, G. Spagnuolo, and M. Vitelli, "Optimization of perturb and observe maximum power point tracking method," *IEEE Trans. Power Electron.*, vol. 20, no. 4, pp. 963–973, 2005.
- [31] W.-J. Gu and K. Harada, "A new method to regulate resonant converters," *IEEE Trans. Power Electron.*, vol. 3, no. 4, pp. 430–439, 1988.
- [32] R. Matsumoto and H. Fujimoto, "Wireless ev charging system using pwm-controlled variable capacitor for maximum power transfer under severe coil misalignment," in *Proc. IEEE Int. Power Electron. Conf. (ECCE Asia)*, 2022, pp. 1476–1480.
- [33] F. Grazian, T. B. Soeiro, and P. Bauer, "Inductive power transfer based on variable compensation capacitance to achieve an ev charging profile with constant optimum load," *IEEE Trans. Emerg. Sel. Topics Power Electron.*, pp. 1–1, 2022.
- [34] U. D. Kavimandan, S. M. Mahajan, and C. W. Van Neste, "Analysis and demonstration of a dynamic zvs angle control using a tuning capacitor in a wireless power transfer system," *IEEE Trans. Emerg. Sel. Topics Power Electron.*, vol. 9, no. 2, pp. 1876–1890, 2021.